MASSIVE STAR EVOLUTION AND SUPERNOVAE

Claes Fransson

October 27, 2005

Contents

1 Pre-supernova Evolution of Massive Stars

1.1 Low mass versus high mass evolution

The evolution of the star is mainly the evolution of the core. This is in turn determined by the temperature and density. In particular, the final stages depend on whether or not the core becomes reaches a temperature high enough for carbon to ignite.

We can separate two qualitatively different behaviors, depending on the value of the core mass M_c. Core masses below M_{Ch} never reach a temperature larger than $T_{c,max}$, while those above can increase their temperature as the core contracts and ignite new fuels. For $M_c > M_{Ch}$ the temperature rises monotonically as $T_c \propto \rho_c^{1/3}$. The division of these two cases occur for $8 - 10$ $M_\odot$, Stars with mass smaller than this only evolves to the helium burning stage, when they become red giants. At this point they loose a large fraction of their hydrogen envelope in a superwind lasting a few $\times 10^4$ years, forming a planetary nebula. The core, forming a white dwarf with a mass of less than the Chandrasekhar mass 1.46 $M_\odot$, consists of mainly oxygen and carbon. Stars with larger mass than $8-10$ $M_\odot$, however, continue their evolution into the more advanced burning stages, and end their lives in a supernova explosion, and finally a neutron star or black hole.

In Fig. 1 this is shown in more detail from evolutionary calculations for stars of different masses. The 1 $M_\odot$ and 2 $M_\odot$ stars become degenerate before He-ignition, while the 7 $M_\odot$ model ignites helium non-degenerately but then evolves into the degenerate regime. In all three cases does the cores not reach a temperature high enough for carbon burning to start. The 15 $M_\odot$ model on the other hand continues to evolve in the partially degenerate regime and the temperature increases monotonically, and passes through all the nuclear burning stages.

In Fig. 2 a more recent calculation of the evolution of a 15 $M_\odot$ and 25 $M_\odot$ star is shown through all evolutionary stages up to silicon burning.

1.2 Advanced nuclear burning stages

In this section we include a brief discussion of the advanced burning stages. For a more complete account of the nuclear physics, as well as the hydrogen and helium stages, see especially Clayton (1967) or Arnett (1996).

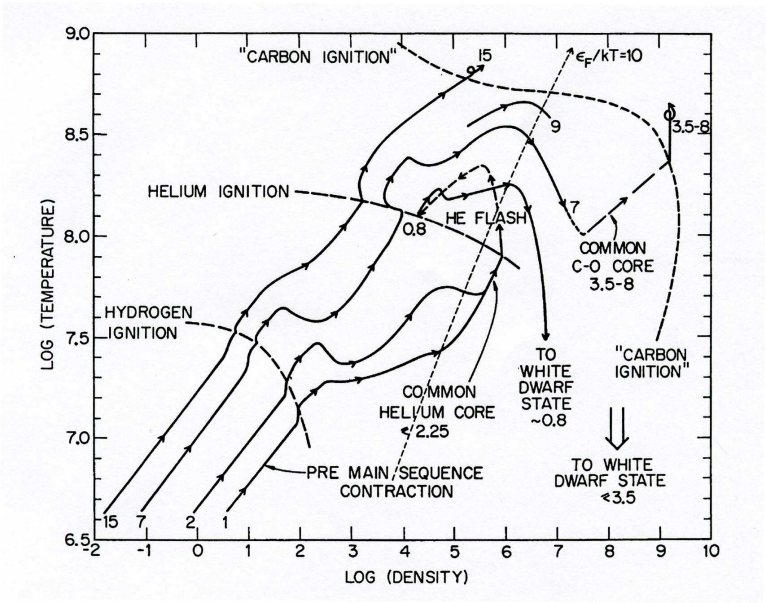

Figure 1: Evolution of the central density and temperature for stars of different masses. (Iben 1974)

1.2.1 Carbon burning

Carbon burning occurs at $(0.6 - 1.2) \times 10^9$ K. The principal reactions occur through the compound nucleus $^{24}\mathrm{Mg}^\star$, which decays as

$$^{12}\mathrm{C} + {}^{12}\mathrm{C} \rightarrow {}^{24}\mathrm{Mg}^\star \rightarrow {}^{24}\mathrm{Mg} + \mathrm{n} - 2.6 \text{ MeV} \quad (1.1)$$

$$\rightarrow {}^{20}\mathrm{Ne} + \alpha + 4.6 \text{ MeV } (\sim 50\%) \quad (1.2)$$

$$\rightarrow {}^{23}\mathrm{Na} + \mathrm{p} + 2.2 \text{ MeV } (\sim 50\%) \quad (1.3)$$

In the interesting temperature range the reaction rate depends on the temperature as $q \propto T^{29}$.

1.2.2 Neon burning

Neon burning occurs in a narrow range at $\sim 1.5 \times 10^9$ K. The first step is photo-disintegration

$$^{20}\mathrm{Ne} + \gamma \rightarrow {}^{16}\mathrm{O} + \alpha \quad (1.4)$$

The next step is that the α particles are partly captured by ^{16}O to form ^{20}Ne, and partly by ^{20}Ne to produce ^{24}Mg, i.e., $^{20}\mathrm{Ne} + \alpha \rightarrow {}^{24}\mathrm{Mg}$. The net

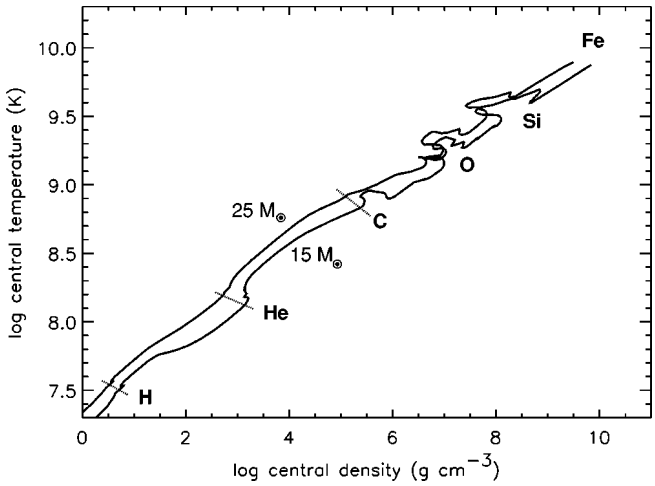

Figure 2: Evolution of the central density and temperature for a 15 $M_\odot$ and 25 $M_\odot$ star. (WHW02)

result of each of these reactions can be summarized as

$$2\ ^{20}\mathrm{Ne} \rightarrow\ ^{16}\mathrm{O} + {}^{24}\mathrm{Mg} + 4.6\ \mathrm{MeV} \tag{1.5}$$

Note, however, that this is only symbolic, and is not a binary heavy ion reaction, like carbon burning. Because of the sensitivity of the α particle abundance to the temperature the reaction rate depends extremely sensitively on the temperature, as $q \propto T^{50}$.

One may ask why neon burning occurs before oxygen burning. The reason is that ^{16}O is a doubly magic nucleus, and has consequently a larger binding separation energy for α particles than neon, 7.2 and 4.7 MeV, respectively.

1.2.3 Oxygen burning

Oxygen can burn either as photo-disintegration, $^{16}\mathrm{O}(\gamma,\alpha)^{12}\mathrm{C}$, or as a fusion reaction, producing Si – S. During hydrostatic burning at $\sim 2 \times 10^9$ K the fusion reaction dominates, while in explosive oxygen burning in connection to the supernova explosion, photo-disintegration and fusion are equally

important. The most important fusion reactions are

$$^{16}\mathrm{O} + {}^{16}\mathrm{O} \rightarrow {}^{32}\mathrm{S}^{\star} \rightarrow {}^{31}\mathrm{S} + \mathrm{n} - 1.5 \text{ MeV } (5\%) \quad (1.6)$$

$$\rightarrow {}^{31}\mathrm{P} + \mathrm{p} + 7.7 \text{ MeV } (56\%) \quad (1.7)$$

$$\rightarrow {}^{30}\mathrm{P} + \mathrm{d} - 2.4 \text{ MeV } (5\%) \quad (1.8)$$

$$\rightarrow {}^{28}\mathrm{Si} + \alpha + 9.6 \text{ MeV } (34\%) \quad (1.9)$$

The main products of oxygen burning are ^{28}Si and ^{32}S. At $\sim 2 \times 10^9$ K the reaction rate depends on the temperature as $q \propto T^{33}$.

1.2.4 Silicon burning

Silicon does not fuse as a heavy ion reaction to ^{56}Ni, but instead melts at $\sim 3.5 \times 10^9$ K by photo-disintegration, due to the extremely energetic radiation density. The resulting nuclei in turn photo-disintegrates to lighter nuclei, etc. In summary,

$$^{28}\mathrm{Si}(\gamma,\alpha)^{24}\mathrm{Mg}(\gamma,\alpha)^{20}\mathrm{Ne}(\gamma,\alpha)^{16}\mathrm{O}(\gamma,\alpha)^{12}\mathrm{C}(\gamma,2\alpha)\alpha \quad (1.10)$$

The result is, however, not only lighter nuclei. The α particles produced by the melting will also be captured by the ^{28}Si to form ^{32}S, which may in turn capture new α particles, etc. The result will be a quasi-equilibrium with successively heavier nuclei. The end result of this depends on the neutron excess η. For small values of $\eta \lesssim 6 \times 10^{-3}$, which is needed to produce the right abundances of the isotopes around the iron peak, the most abundant nucleus is also the most tightly bound nucleus ^{56}Ni (see next section). This radioactive isotope subsequently decays into ^{56}Fe. The fact that this radioactive isotope is main result of the silicon burning is important not only for the nucleosynthesis, but also for the observational properties of all kinds of supernovae.

The reaction rate at $\sim 3.5 \times 10^9$ K goes as $q \propto T^{49}$. The energy release is only one half of that of oxygen burning.

1.3 Nuclear statistical equilibrium

Because of the importance of nuclear statistical equilibrium (NSE) in the Si burning phase, as well as in several other contexts, we discuss it in some detail here.

The Saha equation, relating the number densities of two neighboring ionization stages in ionization balance through

$$n_i + \gamma \leftrightarrow n_{i+1} + e^-, \quad (1.11)$$

is

$$\frac{n_{i+1}n_e}{n_i} = \frac{G_{i+1}g_e}{G_i}\frac{(2\pi m_e kT)^{3/2}}{h^3}e^{-\chi_i/kT} \tag{1.12}$$

where G_i is the partition function of the ion i, g_e the statistical weight of the electron and χ_i the ionization potential.

In exact analogy with this, one can relate the equilibrium densities of two different isotopes in photodissociation balance

$$n_{Z,A} + \gamma \leftrightarrow n_{Z,A-1} + n \tag{1.13}$$

by

$$\frac{n_{Z,A-1}n_n}{n_{Z,A}} = \frac{2G_{Z,A-1}}{G_{Z,A}}\frac{(2\pi m_{Z,A-1}m_n kT)^{3/2}}{h^3 m_{Z,A}^{3/2}}e^{-Q_n/kT} \tag{1.14}$$

where we have used the fact that the statistical weight of the neutron is $g_n = 2$. Q_n is the binding energy of the neutron in the nucleus (Z,A), $Q_n = (m_{Z,A-1} + m_n - m_{Z,A})c^2$. In more compact notation we can write this as

$$\frac{n_{Z,A-1}n_n}{n_{Z,A}} = \frac{2G_{Z,A-1}}{G_{Z,A}}\left(\frac{A-1}{A}\right)^{3/2}\theta\ e^{-Q_n/kT} \tag{1.15}$$

where $\theta \equiv (2\pi m_n kT)^{3/2}/h^3$.

Similarly, we can remove one proton from the nucleus we produced in reaction (1.13) by photodissociation according to

$$n_{Z,A-1} + \gamma \leftrightarrow n_{Z-1,A-2} + p \tag{1.16}$$

producing the next lighter element Z-1. As above we get for this balance

$$\frac{n_{Z-1,A-2}n_p}{n_{Z,A-1}} = \frac{2G_{Z-1,A-2}}{G_{Z,A-1}}\left(\frac{A-2}{A-1}\right)^{3/2}\theta\ e^{-Q_p/kT} \tag{1.17}$$

where $Q_p = (m_{Z-1,A-2} + m_p - m_{Z,A-1})c^2$.

This procedure can now be repeated until we have only protons and neutrons left. Putting these steps together we obtain

$$n_{Z,A} = G_{Z,A}\frac{A^{3/2}n_p^Z n_n^{A-Z}}{2^A}\theta^{1-A}\ e^{Q_{Z,A}/kT} \tag{1.18}$$

where now $Q_{Z,A} = (Zm_p + (A-Z)M_N - m_{Z,A})c^2$ is the total binding energy of the nucleus.

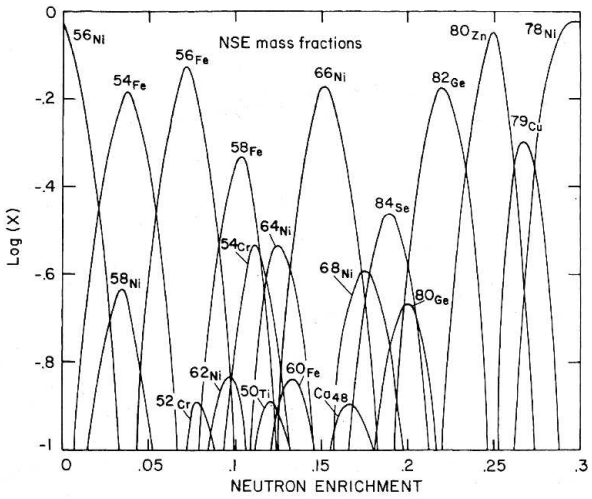

Figure 3: Abundances of iron peak elements at 3.5×10^9 K as function of the neutron excess. From left to right the isotopes are ^{56}Ni, ^{54}Fe, ^{56}Fe, ^{58}Fe. (Hartman, Woosley qnd el Eid 1985)

A particular composition is then characterized by a given value of Y_e or η. Once this is specified all other abundances can then be calculated from the NSE relation Eq. (1.18).

Which nucleus is most abundant in NSE depends on the value of η. In general, for $T \lesssim 10^{10}$ K the most tightly bound nucleus for a given value of η is favored. Consequently, for small neutron excesses one finds that ^{56}Ni, which is an even-even nucleus with $\eta = 0$, is the most abundant nucleus, while at $\eta \sim 0.07$ ^{56}Fe, with $\eta = (30 - 26)/56 = 0.071$, is most abundant. In Fig. 3 we show the isotopic abundances for a few different temperatures as function of η. We see that the abundances do not change appreciably as function of temperature, except for a general decrease in the iron peak abundances, reflecting the shift to ^{4}He, as photo-disintegration of ^{56}Fe becomes important.

1.4 Neutrino cooling

In the advanced burning stages cooling by neutrinos play an increasingly important role. At temperatures of the order of $m_e c^2/k \sim 5 \times 10^9$ K electron pair production by energetic photons becomes possible. In most cases these pairs annihilate into photons, but because the electrons and neutrinos couple through the weak interaction, occasionally a neutrino - anti-neutrino pair

may be produced,

$$e^- + e^+ \rightarrow \nu + \bar{\nu} \tag{1.19}$$

The typical neutrino cross section is

$$\sigma \approx 10^{-44} \left(\frac{E}{m_e c^2} \right)^2 \text{ cm}^{-2}. \tag{1.20}$$

The electron-positron annihilation cross section is of the order of the Thompson cross section, $\sigma_T = 0.665 \times 10^{-24} \text{cm}^2$ (or rather Klein-Nishina at these energies). Therefore the probability for *neutrino pair production* is $\sim 10^{-20}$ of the electron pair annihilation rate.

The neutrino energy loss rate at $T < 10^9$ K is given by

$$\epsilon_\nu \approx 4.9 \times 10^{18} T_9^3 \exp^{-11.86/T_9} \text{ erg cm}^{-3} \tag{1.21}$$

and at $T > 3 \times 10^9$ K

$$\epsilon_\nu \approx 4.5 \times 10^{15} T_9^9 \text{ erg cm}^{-3} \tag{1.22}$$

This clearly illustrates the sensitivity of the neutrino losses to the temperature.

Except for pair production, also other neutrino cooling processes may be important. In particular, the plasma neutrino cooling process and photo-neutrino process are important in many circumstances.

The photo-neutrino process is just pair production of a neutro-antneutrino pair

$$\gamma + e^- \rightarrow e^- + \nu + \bar{\nu}, \tag{1.23}$$

For most massive stars it is the pair annihilation cooling which accounts for most of the cooling, although plasma neutrino cooling is important in especially stars of lower mass.

1.5 Duration of the burning stages

Because of the increasing importance of neutrino losses as the temperature increases because of core contraction, and also the decreasing energy generation per mass, the durations of the burning stages decrease rapidly from thousands of years for carbon burning to days or less for silicon burning. In Tables 1 and 2 we give the duration, as well as the ignition temperature and other parameters, for a 15 $M_\odot$ and a 25 $M_\odot$ ZAMS star, including mass loss (from WHW02). These models include mass loss (see below), explaining the low masses in the table.

Table 1: **Burning stages for a** 15 $M_\odot$ **star (WHW02)**

Fuel	Ashes	T 10^8 K	ρ g cm^{-3}	M $M_\odot$	L 10^3 $L_\odot$	R $R_\odot$	τ yrs
H	He, N	0.35	5.8	14.9	28.0	6.75	1.1×10^7
He	C,O	1.8	1.4×10^3	14.3	41.3	461.	2.0×10^6
C	Ne, Mg, O	8.3	2.4×10^5	12.6	83.3	803.	2.0×10^3
Ne	O, Mg, Si	16.3	7.2×10^6	12.6	86.5	821.	0.73
O	Si, S	19.4	6.7×10^6	12.6	86.6	821.	2.6
Si	Ni	33.4	4.3×10^7	12.6	86.5	821.	18 days

Table 2: **Same as above for a** 25 $M_\odot$ **star**

Fuel	Ashes	T 10^8 K	ρ g cm^{-3}	M $M_\odot$	L 10^3 $L_\odot$	R $R_\odot$	τ yrs
H	He	0.38	3.8	24.5	110.	9.2	6.7×10^6
He	C,O	2.0	7.6×10^2	19.6	182.	1030.	8.4×10^5
C	Ne, Mg	8.4	1.3×10^5	12.5	245.	1390.	5.2×10^2
Ne	O, Mg	15.7	4.0×10^6	12.5	246.	1400.	0.89
O	Si, S	20.9	3.6×10^6	12.5	246.	1400.	0.40
Si	Ni	36.5	3.0×10^7	12.5	246.	1400.	0.73 days

Note in this table the dramatic decrease in the duration of the advanced burning stages, because of increasing neutrino losses in the carbon burning stage and beyond. Also note, while there is only a small decrease in the total mass of the 15 $M_\odot$ star, the 25 $M_\odot$ star ends up with only half of the original ZAMS mass. We will discuss this further later.

After the carbon burning stage the neutrinos dominate the cooling of the core, as Fig. 4 clearly shows.

After carbon burning the diffusion time for the photons is much longer than the duration of these stages, and the core evolves independently from the envelope. Unless some kind of shell flash or similar occurs, the envelope is essentially decoupled from the core.

1.6 Mass loss

Most massive stars experience mass loss to a varying degree. The properties of these winds, however, vary dramatically between the different evolution-

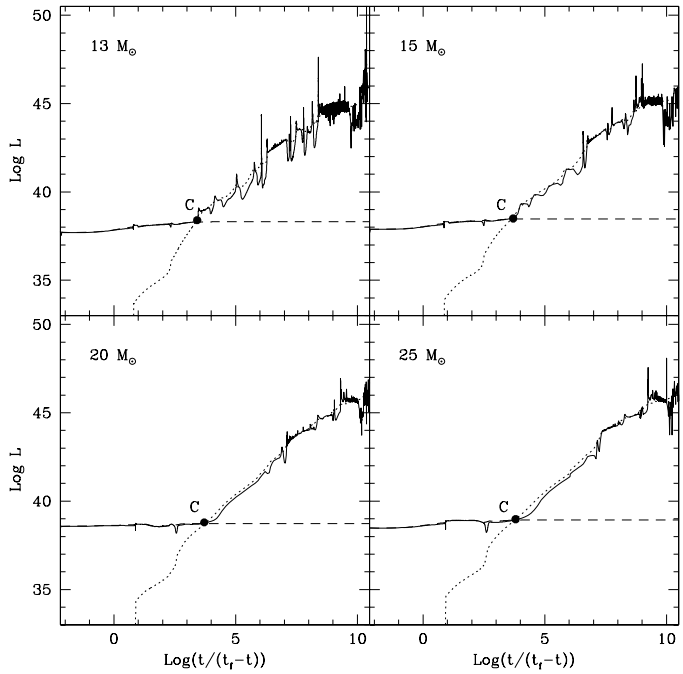

Figure 4: Neutrino luminosity of stars with mass $13 - 25$ $M_\odot$ compared to the nuclear energy generation and the photon luminosity (Limongi et al. 2002).

ary stages. In particular, the wind velocity scales roughly with the escape velocity of the star, which varies by a factor of about a hundred between the blue supergiant, red supergiant, and Wolf-Rayet phases.

In the blue supergiant (BSG) MS phase the winds are radiatively driven through momentum deposition from absorption of the photospheric radiation by the many resonance lines in especially the UV and far-UV. This is a fairly well understood process both theoretically and observationally. Typical mass loss rates are of the order of 10^{-6} $M_\odot$ yr^{-1} and the wind velocities are $1,000 - 3,000$ km s^{-1}.

In the red supergiant (RSG) phase the winds are much less understood. Dust driving is believed to account for most of the momentum input. What initiates the wind (e.g., photospheric shocks connected to pulsations) is, however, not known. Further, it is likely that the star experiences a superwind phase, lasting $\sim 10^4$ yrs in the very last phases of the red supergiant stage. What drives this superwind is somewhat unclear, but pulsational instabilities may be particularly important (see e.g., Heger et al. 1997). Typical

mass loss rates are in the general RSG phase of the order of 10^{-6} $M_\odot$ yr^{-1} and the wind velocities are $10 - 50$ km s^{-1}. In the superwind phase mass loss rates as high as $10^{-4} - 10^{-3}$ $M_\odot$ yr^{-1} may occur. The duration of this phase must obviously be only of the order of a few times 10^4 yrs.

A useful formula which summarizes the mass loss rates on the main sequence and in the red supergiant stage is given by Nieuwenhuijzen & de Jager (1990),

$$\dot{M} = 9.6 \times 10^{-15} \left(\frac{L}{L_\odot}\right)^{1.42} \left(\frac{M}{M_\odot}\right)^{0.16} \left(\frac{R}{R_\odot}\right)^{0.81} \quad M_\odot \ yr^{-1} \qquad (1.24)$$

Finally, in the Wolf-Rayet (WR) phase the wind velocities increase to $2,000 - 5,000$ km s^{-1}, while the mass loss rate is $\sim 10^{-5}$ $M_\odot$ yr^{-1}. The driving of the wind is here to a large extent by radiation on resonance lines, as in the OB star case. The initiation of the wind is, however, not clear, and pulsations may be important for this. Observationally, clumping of the wind is important, with a typical clumping factor of about two. Once this has been corrected for, the mass loss rates are fairly well determined.

The fact that the RSG phase last for $\sim 10^5$ yrs and the WR phase for a comparable period, and that the mass loss rates in these phases are $10^{-5} - 10^{-4}$ $M_\odot$ yr^{-1}, means that stellar winds will have a major influence on the evolution.

1.7 Evolution in the HR diagram

Mass loss is crucial both for the observational properties the appearance of the star and for the internal structure. Because mass loss is increasingly important with mass, the effects increase strongly with mass. In Fig. 5 we show the evolution in the HR diagram of a 60 $M_\odot$ star with and without mass loss. While both stars evolve to the RSG phase, the star without mass loss end its life in this phase. The star with mass loss, however, evolves back to the blue and becomes a hot star, now without any hydrogen envelope. It has become a helium star, or better known as a Wolf-Rayet star. This evolutionary scenario is a general feature for massive stars above some limiting mass, M_{WR}, which is uncertain, but probably in the range $20 - 40$ $M_\odot$, depending on mass loss rates, rotation, metallicity etc. (see below). We therefore have the evolutionary sequence

$$\mathrm{O} \rightarrow \mathrm{BSG} \rightarrow \mathrm{RSG} \rightarrow \mathrm{WR} \qquad (1.25)$$

The most massive stars may loose mass so fast that they never evolve to the RSG stage, but instead evolve as luminous blue variable (LBVs) and then

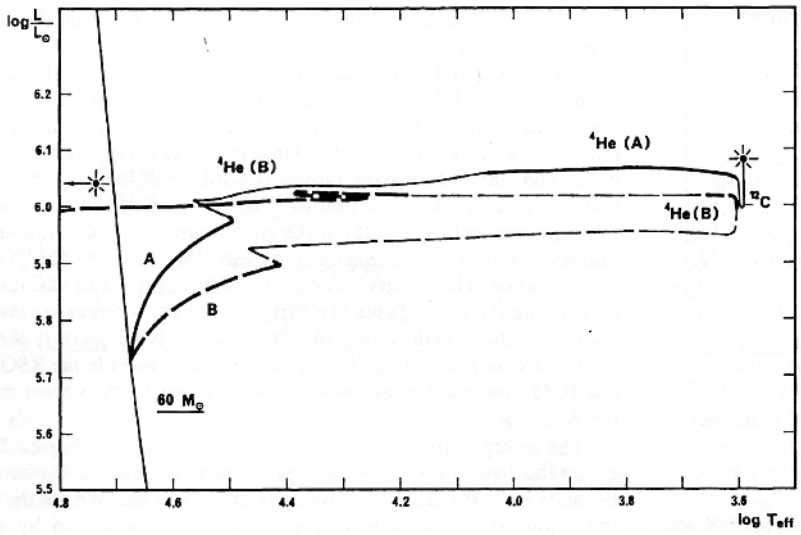

Figure 5: Evolution of a 60 $M_\odot$ star with (dashed line) and without (solid line) mass loss (Maeder 1981)

directly to the WR stage.

$$\mathrm{O} \rightarrow \mathrm{LBV} \rightarrow \mathrm{WR} \tag{1.26}$$

Because mass loss increases with luminosity and mass, $\dot{M} \propto L \propto M^{2-3}$, the effects are most important for the most massive stars. The result is that the final mass before the star collapses is nearly independent of the initial mass! When rotation is taken into account one finds a final mass of $10 - 15$ $M_\odot$ for all masses $\gtrsim 20$ $M_\odot$, as shown in Fig. 6.

1.8 Structure before explosion

The structure of the star just before collapse is extremely important for the outcome of the subsequent phases, including the supernova explosion. In Fig. 7 we show the abundance structure of a 15 $M_\odot$ and a 25 $M_\odot$ star shortly before core collapse. Because of mass loss on the MS and in the RSG phase, ~ 3 $M_\odot$ were lost before the explosion for the 15 $M_\odot$ model, while the 25 $M_\odot$ had lost ~ 12 $M_\odot$, illustrating the increasing importance of mass loss for the massive stars. Except for this, the general structure of the two models are similar.

The first thing to note is the pronounced onion shell structure with a number of distinct zones, reflecting the different burning stages at the

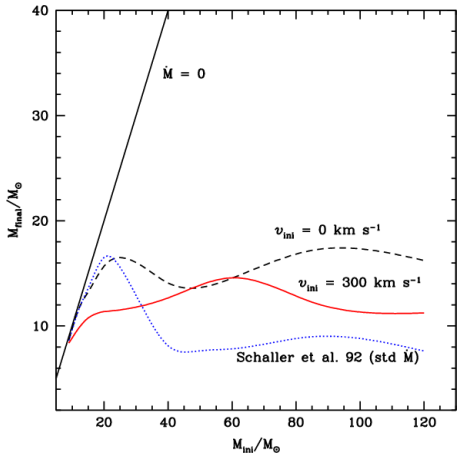

Figure 6: The effects of rotation and mass loss on the final mass of massive stars. The solid line gives the final mass for a ZAMS rotational velocity of 300 km s^{-1}, while the dashed line gives the zero velocity result, only including mass loss (Meynet & Maeder 2003)

time of core collapse. Concentrating first on the 25 $M_\odot$ model, from the surface inwards to $\sim$ 8.2 $M_\odot$ we have the unprocessed hydrogen envelope. We here note that the He mass fraction is roughly twice the original, and is actually higher than that of H. Consistent with this is the high N abundance, depressed O abundance and nearly zero C abundance. This is a typical signature of CNO burning products, which have been brought to the surface by convective mixing of the envelope during the RSG phase. In the 15 $M_\odot$ model this mixing is negligible, but this conclusion is sensitive to factors like rotation and convective treatment.

Inside the hydrogen envelope, the helium mantle has almost the same thickness in mass in both stars. The total mass of He produced is, however, different, because a large fraction of the He from the shell-burning has been mixed with the hydrogen envelope (see above). Besides He, the most important elements are Ne and C. Most of these are the result of He-burning, mixed throughout the He shell.

In terms of nucleosynthesis the most important region is the oxygen zone. The mass of the oxygen core varies strongly with ZAMS mass. For the 15 $M_\odot$ model it is 3.1 $M_\odot$, while it is 7.2 $M_\odot$ for the 25 $M_\odot$ model. The most abundant elements are O ($\sim$ 80%) and Ne ($\sim$ 20%). Also Mg has a substantial abundance in this region. The inner O zone has a large abundance of nuclei resulting from Ne and O burning, in particular Si, S, Ar,

as a result of convective mixing from the O burning shell. These dominate completely in a thin region inside the O zone. The central ~ 1.6 $M_\odot$ consists of iron group elements from Si-burning. Between the iron core and oxygen core are products of oxygen burning and incomplete Si-burning.

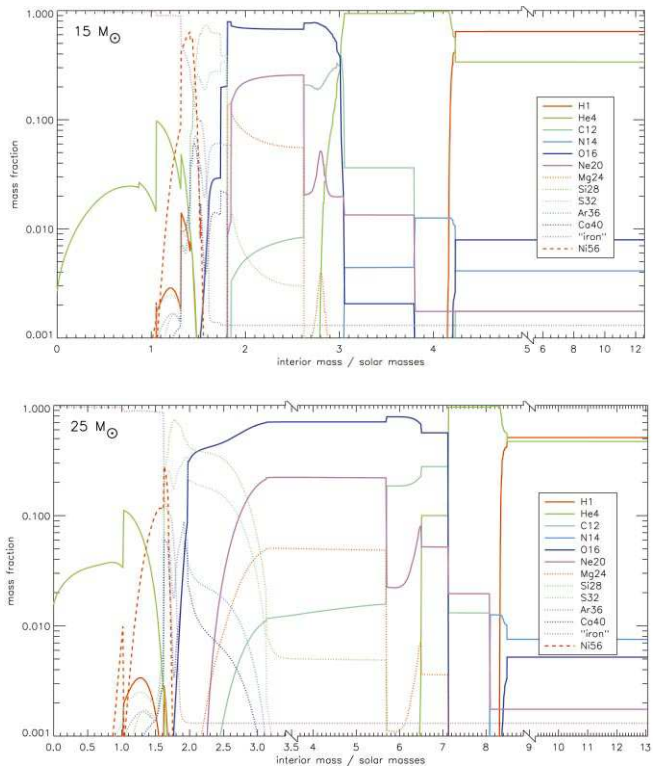

Figure 7: Abundance structure of a 15 $M_\odot$ and 25 $M_\odot$ star shortly before core collapse. (WHW02)

The density structure before core collapse is important for the properties of the supernova explosion. Fig. 8 shows the density as function of mass from the center for stars of different masses. No mass loss has been included in these models, but the general structure including this is quite similar.

One can roughly distinguish three regions. Most of the volume consist of a very extended hydrogen envelope, with radius $\gtrsim 3 \times 10^{13}$ cm containing most of the mass. The mass of this is, not very surprising, sensitive to mass loss. The radius is, however, characteristic of a red supergiant as long, as there is at least ~ 1 $M_\odot$ of hydrogen left.

Next comes the helium mantle with radius $\sim 10^{11}$ cm and density $\sim$

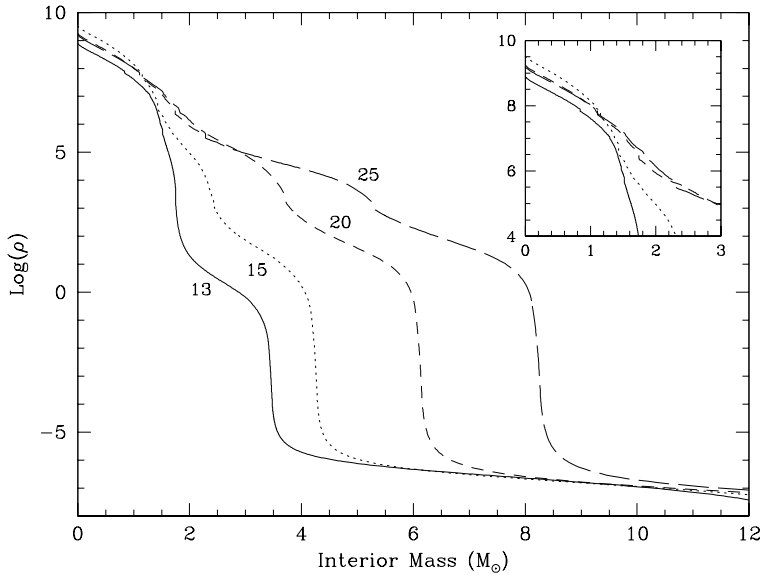

Figure 8: Density structure of four stars with ZAMS $13 - 25$ $M_\odot$ star. (Limongi et al. 2002)

10^2 g cm^{-3}. Inside this there is a gradual increase in the density in the oxygen core. Finally, in the inner ~ 1.5 $M_\odot$ we have the iron core with a radius of only $\sim 3 \times 10^8$ cm and a density $10^7 - 10^9$ g cm^{-3}.

When we compare the structure of the different models, the most apparent differences are the mass of the helium core, and the density gradient outside the iron core. In general the latter becomes less steep as the mass of the star increases. This will be important when we discuss the propagation of the shock wave after the bounce.

The mass of the Fe-core is crucial for whether the explosion will be successful or not. While this mass is only weakly dependent on the ZAMS mass in this interval, $13 - 25$ $M_\odot$, the small difference between 1.29 $M_\odot$ and 1.53 $M_\odot$ for the 13 $M_\odot$ and 25 $M_\odot$ models, respectively, may, however, be crucial for the outcome.

1.9 Triggering of collapse

A self-gravitating body is stable to perturbations as long as its adiabatic index is larger than 4/3 As soon as $\gamma < 4/3$ the star (or core) will collapse.

There are several reasons why the core collapses. Photo-disintegration of Fe into α particles, or even nucleons, require ~ 8.8 MeV per nucleon.

This takes away thermal energy from the core, and thus pressure support. A further reason for instability comes from electron capture on free protons and on bound protons in nuclei,

$$e^- + p \rightarrow \nu_e + n \tag{1.27}$$

The removal of electrons again decreases the pressure in the core.

Once the core becomes unstable it will collapse on roughly a dynamical time scale, $t_{dyn} \sim R/v$, Assuming that the core collapses with the free-fall velocity, V_{ff}, we get

$$t_{dyn} = \frac{R}{V_{ff}} = \left(\frac{R^3}{2GM}\right)^{1/2} \tag{1.28}$$

In terms of the density this is

$$t_{dyn} = \left(\frac{3}{8\pi G\rho}\right)^{1/2} \tag{1.29}$$

At the edge of the iron core the density is $\sim 10^8$ g cm^{-3} when core collapse sets in, and at the center it is $\sim 3 \times 10^9$ g cm^{-3}. Therefore,

$$t_{dyn} = 0.13\ \rho_8^{-1/2}\ \mathrm{s} \tag{1.30}$$

and the collapse time scale is therefore of the order of milliseconds. Hydrodynamical models show that in reality the velocity is only $0.5 - 0.8$ of the free-fall velocity, but as an order of magnitude estimate Eq. (1.30) is sufficient.

1.10 Neutrino trapping

During core collapse neutrinos produced in the core are absorbed and scattered by the nucleons. The most important elastic scattering processes are scattering by free neutrons and protons, and coherent scattering against bound neutrons and protons in nuclei,

$$\nu + n \rightarrow \nu + n \tag{1.31}$$

and

$$\nu + p \rightarrow \nu + p \tag{1.32}$$

and

$$\nu + (Z, A) \rightarrow \nu + (Z, A). \tag{1.33}$$

All three processes are mediated by neutral currents, and were before the Weinberg-Salam-Glashow electro-weak theory not considered. In fact, they make a crucial difference for the neutrino trapping, as we will see. Because of the coherence, the cross section of the last process is not only proportional to A, but to A^2.

In addition to the scattering against the nucleons, *inelastic* scattering against electrons also take place,

$$\nu + e^- \rightarrow \nu + e^- \ . \tag{1.34}$$

The cross section of this is, however, only $\sim 1/600$ of that of the elastic nucleon scattering. Elastic scattering against the nucleons therefore dominate the inelastic scattering against the electrons by a large factor. When we estimate the mean free path to the scattering, we can therefore neglect the electrons. The inelastic scattering may nevertheless be important for thermalizing the neutrinos to the same temperature as the electrons.

For neutrino energies much less than $m_n c^2 \sim 1$ GeV the cross section for the nucleon scattering is

$$\sigma_\nu = \frac{1}{4}\sigma_0 \left(\frac{E_\nu}{m_e c^2}\right)^2 \tag{1.35}$$

where

$$\sigma_0 = \frac{4G_F^2 m_e^2}{\hbar^4} = 1.76 \times 10^{-44}\mathrm{cm}^2. \tag{1.36}$$

The mean free path for scattering is $\lambda_\nu = 1/ < n\sigma_\nu >$, which is an average over the cross sections for these processes. An approximate expression for the mean free path is given by

$$\lambda_\nu \approx 2 \times 10^5 \left(\frac{E_\nu}{10 \text{ MeV}}\right)^{-2} \ \rho_{12}^{-1} \text{ cm} \tag{1.37}$$

The typical neutrino energy is ~ 20 MeV, so the mean free path is only $\sim 0.5 \ \rho_{12}^{-1}$ km.

Scattering is a diffusion process, and from the diffusion equation in spherical geometry one finds that the time for a neutrino to diffuse a radial distance R is

$$t_{diff} = \frac{R^2}{3\lambda_\nu c} \tag{1.38}$$

If we assume a uniform density sphere of mass 1.4 $M_\odot$ and estimate the neutrino energy as the Fermi energy we get $E_\nu \approx E_F = 36.8 \ \rho_{12}^{1/3}$ MeV, and

$$t_{diff} = 5.2 \times 10^{-2} \ \rho_{12} \text{ s} \tag{1.39}$$

The diffusion time scale should be compared to the dynamical time scale, t_{dyn}, from Eq. (1.30),

$$\frac{t_{diff}}{t_{dyn}} = 40\ \rho_{12}^{3/2} \tag{1.40}$$

Therefore, we find that *above a density of* $\sim 10^{11}$ g cm^{-3} *the neutrinos become completely trapped in the core.* This has the consequence that the lepton number will be conserved in the core. If neutrino trapping would not set in, the lepton number would have decreased to a very low level because of beta decay and inverse beta decay (K-capture). This now instead happens **after** the collapse in the explosion phase when the density is low enough.

1.11 Collapse

Because of neutrino trapping, the collapse proceeds almost adiabatically. In Fig. 9 we show the velocity profile of the infalling core at different epochs during the collapse and the formation of the shock. The first curve, (a), corresponds to the final stages of the infall. The central density is $\sim 4.8 \times 10^{13}$ g cm^{-3}. At the next epoch the central density is $\sim 2.6 \times 10^{14}$ g cm^{-3}. The compression at the center generates sound waves which propagate outwards. Curve (c) corresponds to maximum density, $\sim 9.7 \times 10^{14}$ g cm^{-3}. The inner 10 km is now at rest, and from the discontinuity in the velocity curve, it can be seen that the shock has just formed. In (d) the outgoing shock is very obvious. The central density is $\sim 6.9 \times 10^{14}$ g cm^{-3}, and the core is adjusting to its final density $\sim 4 \times 10^{14}$ g cm^{-3}. As we will see in next section, an important point for the survival of the shock is that it is not formed at the center of the star, but close to the outer edge of the core, at a mass of ~ 0.5 M$_\odot$ from the center, or ~ 20 km.

1.12 Energy losses in the shock

The total energy of the shock, as it is launched outside the core, is roughly the binding energy of this, $\sim 5 \times 10^{51}$ ergs. While the initial energy of the shock is large enough to overcome gravity, the problem is that there are severe energy losses behind the shock, which takes away energy from it. These are mainly due to photo-disintegration of iron by the shock and due to neutrino losses in the hot gas behind the shock. Depending on the temperature, the photo-disintegration may proceed all the way to nucleons, or for lower temperature to α particles. Total disintegration of an Fe nucleus to nucleons requires 8.8 MeV per nucleon. Therefore, for each 0.1 M$_\odot$ of iron outside the core $\sim 1.5 \times 10^{51}$ ergs is lost by this process.

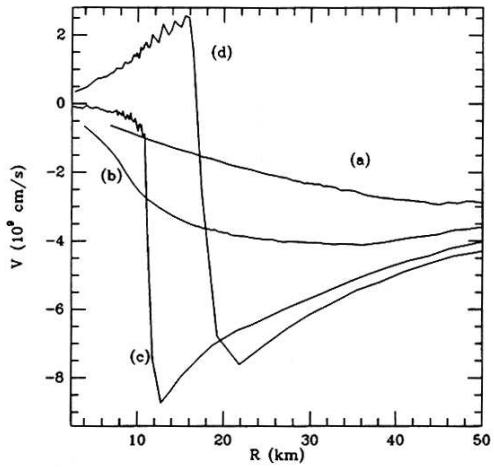

Figure 9: Velocity profile in the core at four epochs during collapse and explosion. Curve a) corresponds to the last epochs of the infall. b) The density at center is close to nuclear. The matter outside is falling in with increasing velocity. c) The infalling mass at the center has been brought to rest, while the accretion is occurring outside. d) The shock has been launched. (Cooperstein & Baron 1990)

Success or failure depends on several factors. The mass of the iron core is crucial, to avoid disintegration losses. The smaller, the better. The maximum mass for an explosion is ~ 1.2 M$_\odot$. This is sensitive to factors like the ^{12}C$(\alpha,\gamma)^{16}$O reaction rate and the treatment of convection. Another important factor is the stiffness of the equation of state. A soft equation of state above nuclear density favors explosion. Unfortunately, this is the most uncertain regime of the equation of state.

Summarizing the current situation, the prevailing view is that this prompt explosion mechanism will probably not work without some additional energy input, or other ingredient, except possibly for stars of mass $\lesssim 12$ M$_\odot$.

1.13 Neutrino heating

In a now classical computer run, Jim Wilson let one of his apparently unsuccessful simulations run for a much longer time than before. When he looked at the result he saw, to his surprise, that the stalled shock had now become a successful one due to the late energy input from the neutrinos from the explosion and the newly formed hot proto-neutron star.

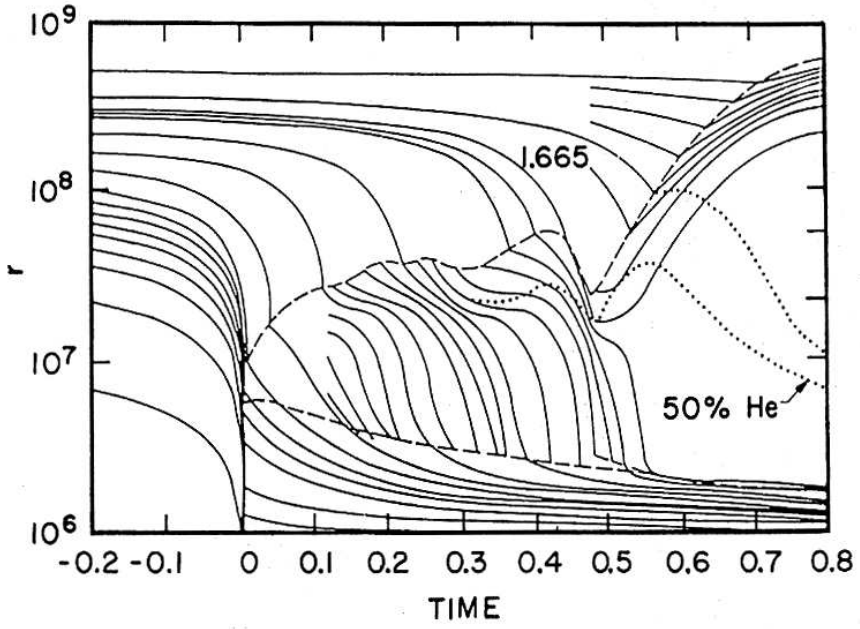

Figure 10: Trajectories of different mass shells for Jim Wilson's successful explosion model. The upper dashed line gives the position of the shock, while the lower is that of the neutrino photosphere. The dotted line marks the region where the abundance of He is 50%. Note the revival of the shock at 0.55 s due to neutrino heating (Bethe & Wilson 1985).

In Fig. 10 we show the resulting mass locations as function of time for this simulation. As we see, the collapse occurs on a time scale of a few tens of milliseconds. The shock forms at a distance of $\sim$ 100 km from the center. This expands, but because of energy losses it looses speed, and after $\sim$ 0.1 s it is almost stalled. Accretion continues, and normally one would consider this a failed explosion. However, because of the longer than normal simulation, we see that at $\sim$ 0.5 s the shock suddenly gets new energy and rapidly expands out of the core. At that point the density at the shock is low enough for losses to be negligible, and a the result is a healthy explosion.

Although successful, these simulations were based on an unrealistic equation of state above nuclear density, as well as other deficiences. Nevertheless, what was most important was that they pointed out the importance of neutrino heating and the consequences of this on a long time scale. We will now discuss the details of this mechanism in more detail.

The proto-neutron star formed by the collapse cools by an enormous flux of neutrinos on a time scale given by the neutrino diffusion time scale t_{diff}, given by Eq. (1.39), but now with $\rho \sim 2 \times 10^{14}$ g cm^{-3}. Finally, as the density decreases at the boundary of the iron core, the density will be low enough for the neutrinos to escape freely. One can therefore, in analogy with the photosphere, define a *neutrino-sphere*. As these propagate out through the shocked gas, they will scatter and be absorbed by the nucleons.

The most important heating processes are

$$\bar{\nu} + p \rightarrow e^+ + n \tag{1.41}$$

and

$$\nu + n \rightarrow e^- + p \tag{1.42}$$

The temperature behind the shock is set by the dis-integration of Fe. For each nucleon this costs a binding energy E_{bind}. Because the cooling decreases faster than the heating, there will be a radius where heating and cooling balance, often referred to as the gain radius. Inside of this there is a net cooling by the neutrinos, while outside there is a net heating. This is summarized in Fig. 11.

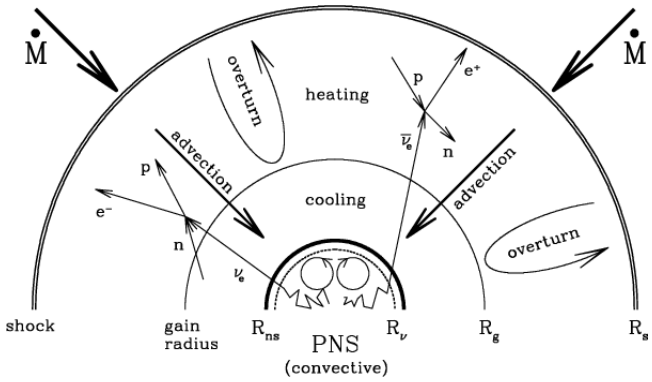

Figure 11: Schematic picture of the different regions close to the neutron star (Janka 2001)

The neutrino heat input is probably crucial for the outcome of the explosion. Just outside the gain radius the matter is heated to a high temperature, decreasing outwards. This therefore induces a strong entropy gradient outwards, leading to convection. The large scale convective motions transport entropy (hot gas) to the region close to the shock and can therefore re-energize the shock (see Fig. 10 and Fig. 12). At the same time low entropy

(cool) gas sinks inward, inside the gain radius. There it will be heated by the neutrinos. This compensates the iron dis-integration losses, and if efficient enough, can cause the shock to survive through the whole iron core.

The efficiency of the late heat input mechanism depends naturally on the neutrino luminosity from the proto-neutron star. The neutrino emission is a consequence of the de-leptonization of the proto-neutron star. The ν_e and $\bar{\nu_e}$ are produced by $e^- + p \rightarrow \nu + n$ and $e^+ + n \rightarrow \bar{\nu_e} + p$, while $e^+ + e^- \rightarrow \bar{\nu_i} + \nu_i$ are responsible for the production of μ and τ neutrinos, by roughly equal numbers.

Taking all these ingredients together, the increased neutrino luminosity from the proto-neutron star, the neutrino heating of the gas of the matter outside the neutron star and the convective motions behind the shock one has in some simulations been able to obtain an explosion. However, several of these successful attempts have weaknesses in the form of the treatment of the neutron star cooling, the radiative transfer of the neutrinos or the equation of state. It is therefore to early to make any conclusions of the success of this mechanism. In addition, there are other ingredient. like magnetic fields and rotation, which have only been included in simplified models. They may, however, be crucial for the outcome. In particular, the gamma-ray bursts may indicate the necessity to include these effects.

1.14 Explosive nucleosynthesis

If the shock has managed to escape the iron core, the density decreases rapidly, and with that the dis-integration and neutrino losses. There will still be some explosive nucleosynthesis in the silicon and inner parts of the oxygen shell, but this only adds a small amount of energy to the shock. After this the shock will propagate through the whole star and disrupt this. As the shock reaches the surface the hot photons behind the shock are released and one observes the explosion. This is however several hours after the collapse of the core.

As the shock wave propagates through the silicon and oxygen rich gas close to the iron core, the temperature behind the shock will be high enough for explosive nucleosynthesis to take place in these regions. This burns most of the Si and S into nuclear statistical equilibrium, (see Fig. 13).

During the first seconds after the core bounce some from the observational point of view most important isotopes are formed. Close to the border between the neutron star and the ejecta the explosive nucleosynthesis occurs in conditions close to NSE. As we saw in §1.3, it is therefore not surprising that the most abundant nucleus is ^{56}Ni. The exact mass of ^{56}Ni, which will

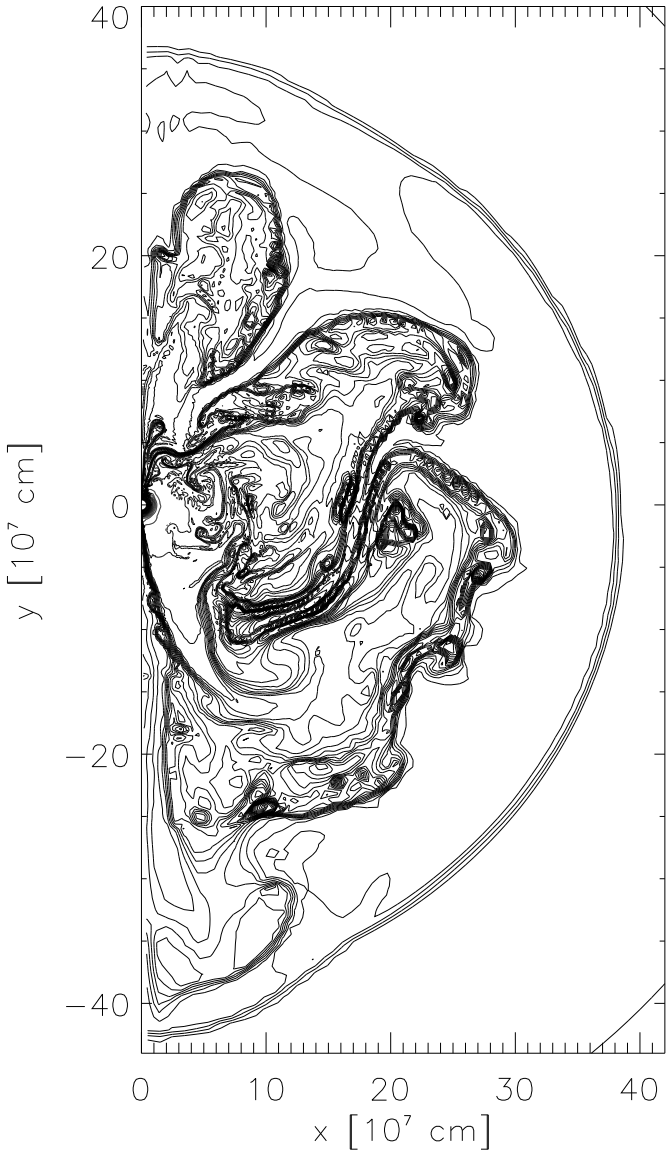

Figure 12: Two-dimensional simulation of the explosion at 0.38 s after core bounce. The contours show the entropy distribution. The shock is at 3800 km. Note the bubbles of neutrino heated gas, and the down drafts of sinking cooler gas. (Janka & Müller 1996)

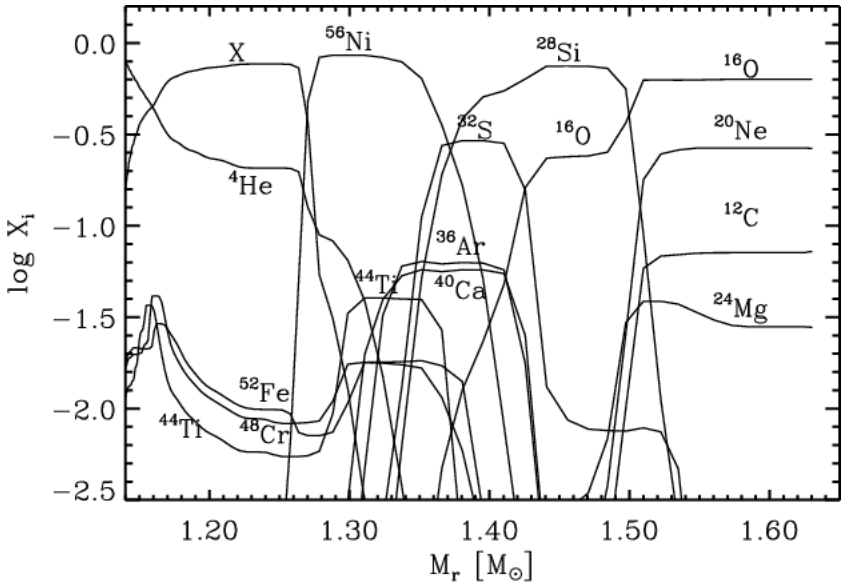

Figure 13: Explosive nucleosynthesis in the central region (Kifonidis et al. 2003).

be ejected, depends sensitively on where the split is between the the matter falling into the neutron star and that expanding out. This is usually known as the 'mass cut'. Typically, the ^{56}Ni mass is ~ 0.1 M$_\odot$, but this can vary by a large factor, both upwards and downwards.

In addition to ^{56}Ni, substantial amounts of ^{57}Ni and ^{44}Ti are created. The exact abundances of the three radioactive isotopes depend on the density, temperature and neutron excess. Therefore, a determination of these abundances provides a useful probe of the conditions at the time of the explosive nucleosynthesis, during the first seconds of the explosion.

Outside the silicon core, in the inner oxygen shell, the shock velocity and density are still high enough for the inner parts of the oxygen core to be transformed into Si/S. At this point the density becomes too low for any significant nucleosynthesis to take place. Outside of the inner oxygen shell, the composition just before core collapse is almost unaffected by the explosion. Summarizing the explosive nucleosynthesis, the most important elements affected by this is oxygen and elements heavier than this.

In addition to these elements, which account for most of the newly created elements in terms of mass, there is also a further process, which is extremely important for the elements beyond the iron peak. This relays on

the fact that close to the mass cut, where the density and temperature is high, the abundance of free neutrons is also high. This high neutron flux can be absorbed by the different abundant iron group nuclei in this region, which leads to the build up of heavier, neutron-rich isotopes. These are usually unstable to especially beta decay, which creates more stable isotopes of the same mass, but higher charge. This process is known as the r-process, r for rapid.

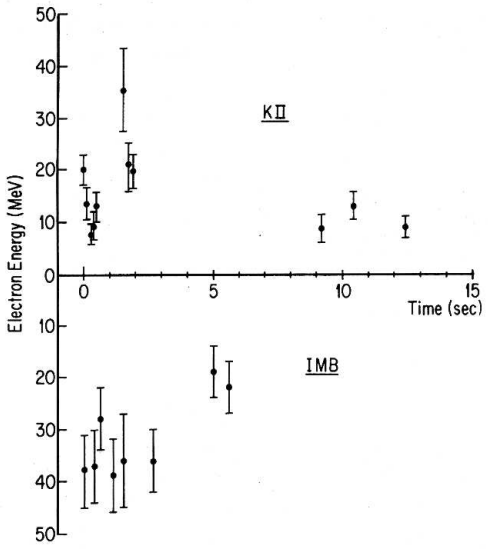

Figure 14: Energy versus arrival time for the detected neutrinos in the Kamiokande II and IMB detectors. (Burrows 1988).

2 Observables of core collapse supernovae

2.1 Neutrinos from SN 1987A

The most unique observation of SN 1987A is the first observation of neutrinos from outside of the solar system. Although already Chiu and Colgate & White in the 1960's had predicted that most of the gravitational energy in the collapse would emerge as neutrinos, the flux from supernovae at 'normal' distances is too low for the current (and probably next) generation of neutrino detectors. However, the small distance to SN 1987A, 50 kpc, meant the the flux was $\gtrsim 10^4$ larger than from a supernova in even the closest galaxies outside the Local Group.

As soon as the news of the discovery of SN 1987A came, the different teams looked at the registration journals of the most sensitive detectors, Kamiokande II in Japan and IMB (Irwine – Brookhaven – Michigan) in Ohio. To their satisfaction they saw a clear signal at exactly the same time, February 23 at 07:35:41 UT. Fig. 14 shows the energies of the individual electrons produced by the neutrinos, which approximately corresponds to a neutrino energy given by $E_\nu \approx E_e + 2$ MeV.

The total energy in the form of neutrinos is straightforward to calculate,

and was predicted long before SN 1987A. Because the kinetic energy of the shock is less than a percent of the total energy, what is emitted is just the binding energy of the neutron star formed. For a uniform density this is

$$E_b = \frac{3}{5}\frac{GM^2}{R} = 3.1 \times 10^{53} \left(\frac{M}{1.4\ \mathrm{M}_\odot}\right) \left(\frac{R}{10\mathrm{km}}\right)^{-1} \mathrm{ergs} \qquad (2.1)$$

Note that we here should use the radius of the cool neutron star $10-20$ km. A more accurate calculation, taking the non-uniform density distribution into account, gives a similar result.

The duration of the burst is set by the diffusion time scale of the neutrinos as the proto-neutron star is deleptonized and is cooling down. The mean free path from Eq. (1.37) is therefore $\sim 10^6 \rho_{14}^{-1} (E_\nu/1\ \mathrm{MeV})^{-2}$ cm. Using a constant density for the proto-neutron star with mass $\sim 1.4\ \mathrm{M}_\odot$, we have $\rho \approx 2.5 \times 10^{13} (R/30\ \mathrm{km})^{-3}$. Using these expressions in the equation for the diffusion time, Eq. (1.38), we get

$$t_{diff} \approx 0.2 \left(\frac{R}{30\ \mathrm{km}}\right)^{-1} \left(\frac{E_\nu}{100\ \mathrm{MeV}}\right)^{2}\ \mathrm{s}. \qquad (2.2)$$

Typically, the neutrino energies are of the order of 100-200 MeV in the inner core.

In reality, the density in the center is higher than the mean density used above, and the neutrino energies also vary by a large factor, so this number should only be taken as indicative. The fact that it is much larger than the dynamical time scale, however, shows the importance of the neutrino diffusion. More accurate calculations show that the neutrinos diffuse out on a time scale of ~ 2 s.

Despite the high interior temperature the neutrinos which escape have a temperature of only $T_\nu \sim 4-5$ MeV, corresponding to a mean energy $< E_\nu > \sim 3\, T_\nu \sim 10-15$ MeV. Because of the high temperature and trapping an approximately equal number of all six neutrino species, $\nu_e, \bar{\nu_e}, \nu_\mu, \bar{\nu_\mu}, \nu_\tau$, and $\bar{\nu_\tau}$ are produced by pair annihilation, the plasmon process and nucleon bremsstrahlung. The energy in each of the neutrinos is therefore $\sim 6 \times 10^{52}$ ergs.

The Kamiokande II and IMB detectors are both water Cherenkov detectors, shielded by several 1000'nds of meter of rock. The total amount of water in these are 2140 tons for Kamiokande II and 6800 tons for IMB. Only electron neutrinos are detected with these water detectors. This occurs through absorption on the protons in the water

$$\bar{\nu_e} + p \rightarrow e^+ + n \qquad (2.3)$$

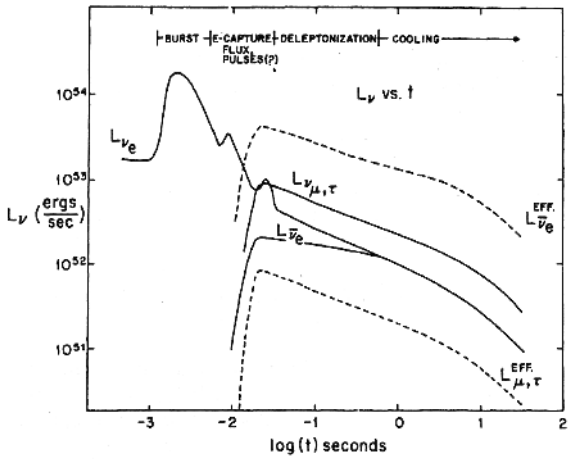

Figure 15: Approximate neutrino luminosities of the different neutron species. Note the logarithmic time scale. (Burrows 1984).

and elastic scattering including all neutrino species, $i = e, \mu, \tau$,

$$\nu_i + e^- \rightarrow \nu_i + e_i^- \tag{2.4}$$

The second reaction has a cross section which is only $\sim 5\%$ of that of the first reaction, which therefore dominates. The neutrino detectors are not sensitive to neutrinos below ~ 7 MeV for Kamiokande II and below ~ 19 MeV for IMB.

To compare the detected signal with the predicted one has to convolve the detector sensitivity with the calculated spectrum. Because of the small numbers (19 neutrinos in total) one compares the predicted curves with the cumulative number of neutrinos detected.

The average observed temperature of the neutrinos is $3 - 5$ MeV, and agrees well with that estimated before the explosion. A recent calculation of the mean energy, $< E_\nu > \sim 3\, T_\nu$. The shorter duration of the IMB signal, which has a higher threshold, actually gives some indication that the source is cooling.

2.2 Supernova classification

The classification of supernovae into different types and subtypes is basically an empirical scheme, based on spectral features and light curves. However,

it turns out that this classification also corresponds to important physical differences between them.

Most SNe are discovered shortly after explosion when they are near maximum luminosity. It is therefore important to be able to distinguish the different types from the early spectrum. In Fig. 16 we show a collection of spectra representing the most important types.

The observationally most obvious difference between various SNe is whether or not they have any hydrogen features in their spectra. Type I SNe are defined as those without and Type II as those with Hα. A closer examination, however, shows that there are important differences within both of these classes. The most important are between the extremely heterogenous Type I's. These are shown as the top and lower two spectra in Fig. 16. While neither of them have any trace of Hα, the observational distinction is that the Type Ia's have a strong Si II λ6150 line, while the Type Ib's and Ic's lack a strong feature at this wavelength. The distinguishing feature between the Ib's and Ic's is the presence of He I lines in the former, while the Ic's lack any trace of helium.

While the differences between the Ia's and Ib/c's seem marginal, it turns out that they originate from completely different explosion mechanisms. The Ia's are thermonuclear explosions of white dwarfs, completely disrupting the star, while the I b/c SNe and the Type II's are core collapse explosions of massive stars, leaving a neutron star or black hole.

This distinction can somewhat better be understood from an examination of the spectra at late epochs. Fig. 17 shows a collection of spectra taken 5 months after explosion. Unfortunately, however, no Type Ib is included, but they are qualitatively similar to the Type Ib's. Now the difference between the Ia's and Ib/c SNe become very large. While the Ia spectra are dominated by [Fe II], [Fe III] and [Co III] features, the most prominent features in the Ic spectrum are due to [O I], [Mg I] and [Ca II], with only weak iron lines. Also the Type II's have late spectra where the same lines are strong, although they tend to appear later than for the Ib/c's.

One can now start to appreciate the physical difference between these classes. The presence of substantial amounts of oxygen, magnesium and calcium is characteristic of the processed regions of a massive star, The Type Ia spectra with only weak features of lines from these elements and strong lines of iron are more typical of matter which has undergone complete burning to nuclear statistical equilibrium. The treason that the Type Ib/c's lack hydrogen is most likely because they have lost their hydrogen envelopes, either as a result of mass loss or binary mass exchange. The progenitors are therefore believed to be Wolf-Rayet stars. A more quantitative confirma-

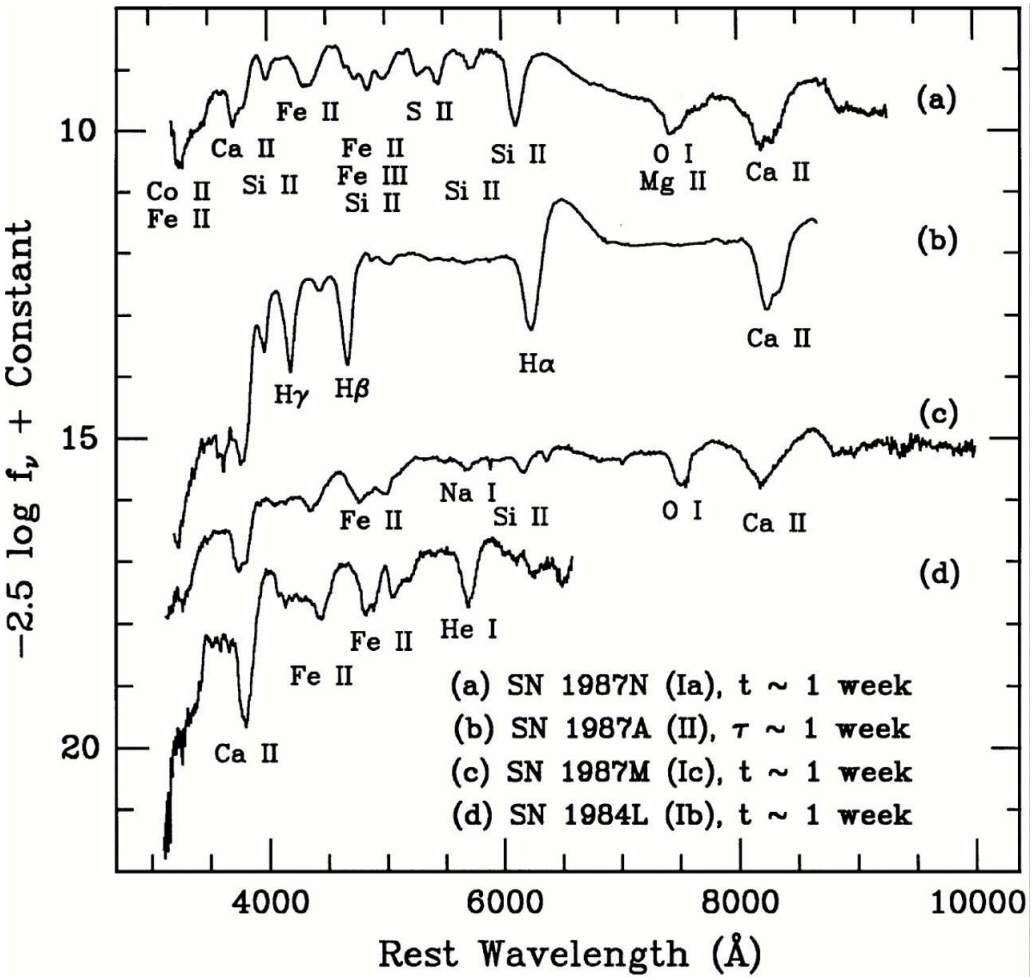

Figure 16: Spectra of different supernova types one week after explosion (Filippenko 1997).

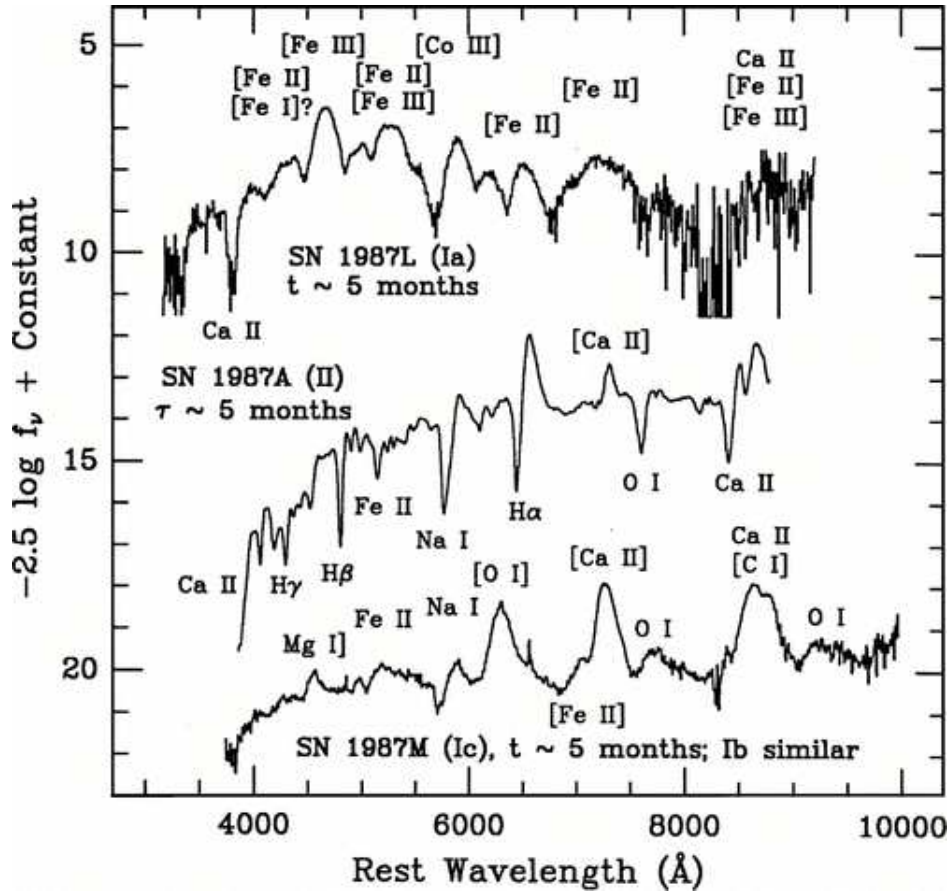

Figure 17: Spectra of different supernova types 5 months after explosion (Filippenko 1997).

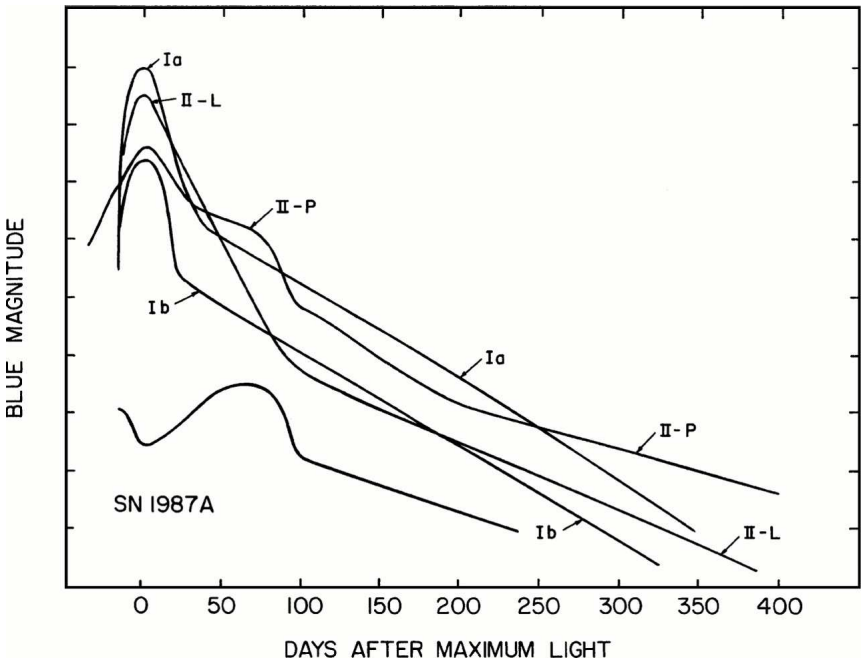

Figure 18: Light curves of different supernova types (Filippenko 1997).

tion of this, requires a much more detailed analysis of their spectra. This, however, completely confirms these conclusions.

While the previous classification has only been discussed from the spectra, there are also important differences with regard to the light curves of the different SN types. In Fig. 18 we show light curves representative of the different types. Here the Type Ia and Type Ib/c curves mainly differ in terms of absolute luminosity. For the first two months they are characterized by a bell shaped peak, occurring 2-3 weeks after explosion. They then have a nearly linear decline in a time - magnitude plot for the rest of the evolution. However, while the Type Ia's are highly standardized, there is a large dispersion within the Type Ib/c curves, both in absolute luminosity and in the shape. In particular, the rate of decline after $\sim$ 50 days differ considerably.

While the Type II's have a fairly large range of light curves, one can distinguish two main types. The IIP's which are the most frequent, are characterized by a fairly fast rise to a peak. After a decline by a magnitude or so, they then stay at nearly constant magnitude for $\sim$ 100 days. This is the reason for the P = plateau. After this there is a drop by a magnitude

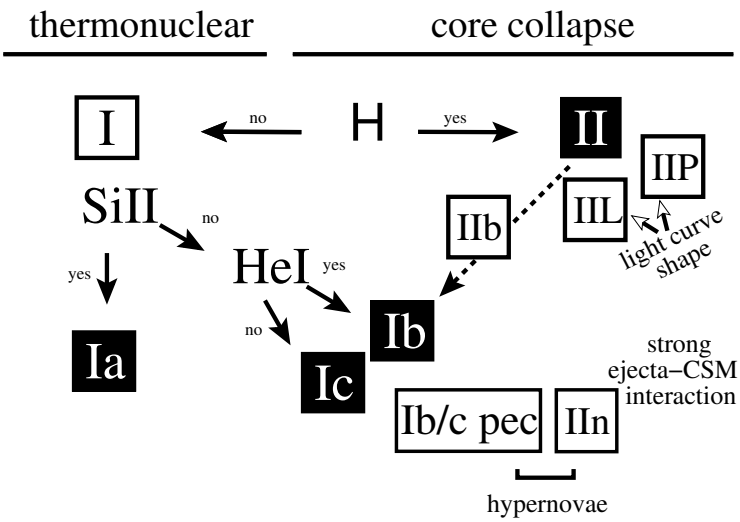

Figure 19: Classification scheme based on spectra and light curves of different kinds of supernovae (Turatto, 2003).

or more, and then they decline with a fairly uniform rate of ~ 1 magnitude per 100 days.

A less frequent class are the Type IIL's, where the L stands for linear. The plateau is here lacking and the linear decline sets in shortly after the peak. Usually, the Type IIL's are considerably brighter in absolute luminosity than the Type IIP's. Spectroscopically, the Type IIL's have already at early epochs a strong Hα line in emission, while Hα has usually a classical P-Cygni profile in the Type IIP's.

In addition to theses main classes, there are several other subtypes, with more or less distinct properties. This is usually connected to interacting with a dense circumstellar medium. In Fig. 19 we summarize the whole SN classification scheme, and we will now discuss the physical interpretation of these characteristics, and the differences between the various types.

2.3 Radioactivity

As we saw in §**??**, the explosive nucleosynthesis in the silicon core resulted in several radioactive isotopes, the most important being ^{56}Ni, ^{57}Ni and ^{44}Ti. All of these have comparatively short half-lives, and the decays of these elements can therefore be directly observed, and are in fact crucial for the observability of the supernova. The decays are characterized by either

the half-life, $t_{1/2}$, or the exponential decay time scale, τ. It is easy to see that $\tau = t_{1/2}/\ln 2$.

^{56}Ni decays on a time scale of $\tau = 8.8$ days by electron capture as

$$^{56}\mathrm{Ni} \rightarrow {}^{56}\mathrm{Co} + \gamma \ . \tag{2.5}$$

In this process it emits gamma-rays with energies 0.158 – 0.812 MeV (see Fig. 20). The ^{56}Co isotope resulting from this decay is, however, not stable either, but decays by electron capture or by positron decay according to

$$^{56}\mathrm{Co} \rightarrow {}^{56}\mathrm{Fe} + \gamma \tag{2.6}$$

$$\rightarrow {}^{56}\mathrm{Fe} + e^{+} \tag{2.7}$$

The first decay occurs in 81% of the cases and the second in the remaining 19%. In terms of energy going into gamma-rays and positrons these numbers are 96.4% and 3.6%, respectively. The strongest gamma-ray lines are at 0.847 MeV and 1.238 MeV. The average positron energy is 0.658 MeV. Similarly, ^{57}Ni decays by electron capture as

$$^{57}\mathrm{Ni} \rightarrow {}^{57}\mathrm{Co} + \gamma \tag{2.8}$$

with a very short decay time $\tau = 52$ hours. The more interesting decay is

$$^{57}\mathrm{Co} \rightarrow {}^{57}\mathrm{Fe} + \gamma \tag{2.9}$$

with $\tau = 390$ days.

Finally, ^{44}Ti decays first to ^{44}Sc on a time scale of ~ 89 years.

$$^{44}\mathrm{Ti} \rightarrow {}^{44}\mathrm{Sc} + \gamma \tag{2.10}$$

and then rapidly ($\tau = 5.4$ hours) to

$$^{44}\mathrm{Sc} \rightarrow {}^{44}\mathrm{Ca} + \gamma \tag{2.11}$$

$$\rightarrow {}^{44}\mathrm{Ca} + e^{+} \tag{2.12}$$

(see Fig. 21).

The result of these radioactive decays are either gamma-rays or positrons. The gamma-rays are scattered by the electrons in the ejecta through Compton scattering. In each scattering they loose roughly half of their energy to the electrons. Because the energy of the gamma-rays are initially in the MeV range, much higher than the binding energies of the bound electrons in the atoms, both free and bound electrons contribute to the scattering.

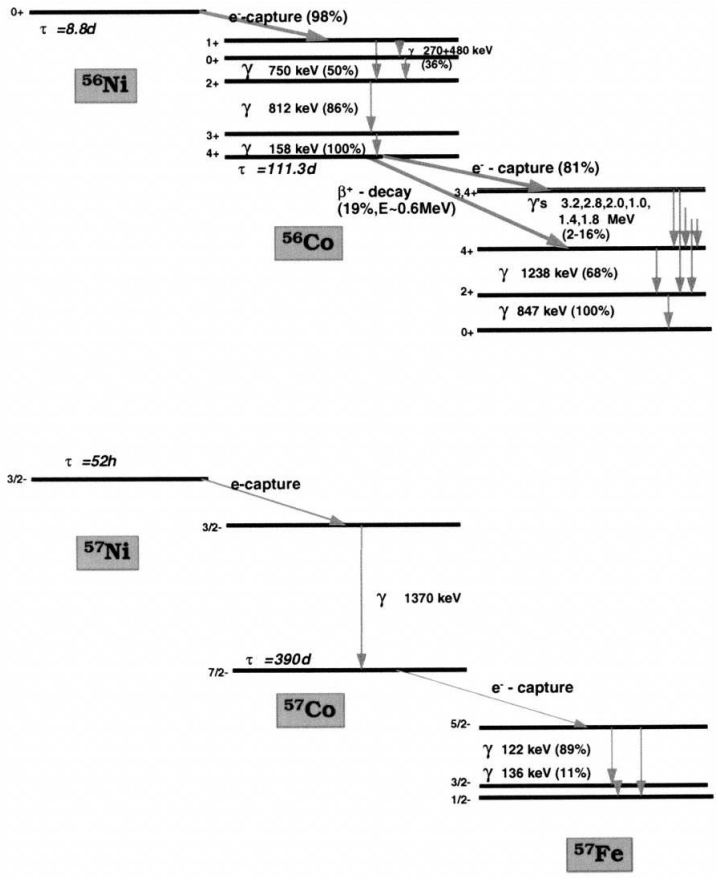

Figure 20: Transitions in the ^{56}Ni and ^{57}Ni decays (Diehl & Timmes 1998).

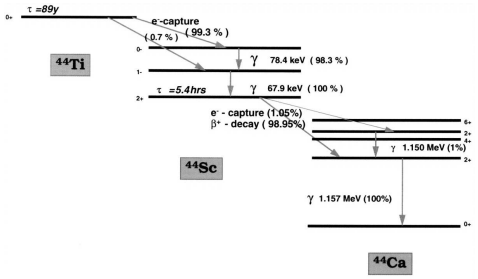

Figure 21: Transitions involved in the ^{44}Ti and ^{44}Sc decays (Diehl & Timmes 1998).

This down-scattering of the gamma-rays continues until the cross section for photoelectric absorption is larger than the Compton cross section, which occurs at an energy of $\sim 10 - 100$ keV, depending on the composition. The most important element for the photoelectric absorption is iron.

The total gamma-ray luminosity from the various decays is given by

$$L_\gamma = \quad 1.27 \times 10^{42} \left(\frac{M(^{56}\mathrm{Ni})}{0.1\ \mathrm{M}_\odot} \right) e^{-t/111.3^{\mathrm{d}}} + \tag{2.13}$$

$$6.9 \times 10^{38} \left(\frac{M(^{57}\mathrm{Co})}{5. \times 10^{-3}\ \mathrm{M}_\odot} \right) e^{-t/390.^{\mathrm{d}}} + \tag{2.14}$$

$$4.1 \times 10^{36} \left(\frac{M(^{44}\mathrm{Ti})}{10^{-4}\ \mathrm{M}_\odot} \right) e^{-t/89.^{\mathrm{yrs}}} \mathrm{erg\,s^{-1}}, \tag{2.15}$$

and the positron input by

$$L_+ = \quad 4.44 \times 10^{40} \left(\frac{M(^{56}\mathrm{Ni})}{0.1\ \mathrm{M}_\odot} \right) e^{-t/111.3^{\mathrm{d}}} + \tag{2.16}$$

$$1.3 \times 10^{36} \left(\frac{M(^{44}\mathrm{Ti})}{10^{-4}\ \mathrm{M}_\odot} \right) e^{-t/89.^{\mathrm{yrs}}} \mathrm{erg\,s^{-1}} \tag{2.17}$$

2.4 Light curves

2.4.1 The diffusion phase of the light curve

After shock breakout the radiation will leak out on a diffusion time scale. We have already estimated this in Eq. (1.38), which we write as

$$t_{diff} = \frac{3R^2 \rho \kappa}{\pi^2 c} \tag{2.18}$$

This should be compared to the expansion time scale $t = R/V$. Taking the opacity to be that of Thompson scattering, $\kappa = 0.4\ \mathrm{cm^2 g^{-1}}$, and assuming a uniform density for the envelope we get

$$\frac{t_{diff}}{t_{exp}} = 1.9 \left(\frac{M}{\mathrm{M}_\odot} \right) \left(\frac{V}{10^4\ \mathrm{km\ s^{-1}}} \right) \left(\frac{R}{10^{15}\mathrm{cm}} \right)^{-2} \tag{2.19}$$

For a typical mass of 10 $\mathrm{M}_\odot$ we therefore find that not until the supernova has expanded to $R_{peak} \sim 4 \times 10^{15}$ cm, after $t_{peak} = R/V \sim 40$ days, can the radiation leak out faster than the ejecta expand. This is analogous to the neutrino trapping discussed in §1.10, although in this case it is expansion, rather than collapse.

Before t_{peak} the expansion is nearly adiabatic. Because the ejecta is radiation dominated it behaves as a $\gamma = 4/3$ gas, and the total thermal energy behaves like

$$E_{int} = (\gamma - 1)^{-1} pV = 3K\rho^{4/3}V \propto \rho^{1/3} \propto R^{-1} \tag{2.20}$$

Therefore, if the progenitor has a radius R_0, the internal energy has decreased by a factor R_{peak}/R_0 once the photons can leak out. A small initial radius therefore means that almost all the internal energy produced by the shock has been lost into adiabatic expansion, i.e., to kinetic energy. If the thermal, shock energy was the only source of energy, supernovae coming from this kind of stars would be very faint. A red supergiant, on the other hand, could be bright for weeks just from the thermal shock energy.

Besides the thermal energy from the shock, there is one more important source for the light curve. As we saw in §2.3, the radioactive isotopes created in the explosion give rise to gamma-rays and positrons as they decay. These are loosing their energy in the ejecta, thermalizing their energy into UV and soft X-ray photons, and therefore acts like an additional energy source. In the same way as the thermal energy from the shock, the photons undergo scatterings in the ejecta and only leak out when the diffusion time scale becomes comparable to the expansion time scale. The difference compared to the shock energy is, however, that this source is not affected by adiabatic expansion. The number of radioactive nuclei, of course, remain the same independent of the expansion. Therefore, even if nearly all the internal heat has been lost in the expansion, radioactivity provides a source for the light curve even at late times.

2.4.2 The late light curve and radioactive isotopes

After the peak diffusion plays a steadily decreasing role, and the light curve becomes simpler. This is in particular the case if we consider the bolometric light curve, i.e., the frequency integrated light curve. In this case the emitted luminosity is just the instantaneous gamma-ray and positron energy absorbed by the ejecta.

If we neglect the scattering in space and energy of the gamma-rays and just consider it as an absorption process, which is a reasonable approximation, although not very accurate, we can calculate the bolometric light curve just from the absorbed energy. As an averaged opacity one can for ^{56}Ni and ^{56}Co use $\kappa_\gamma = 0.06Z/A$ cm^{2}g^{-1}, where Z/A is the average charge to mass ratio of the ejecta. The positrons have a considerably smaller mean free path, and they can be considered to be stopped and annihilate on the same

spot as the radioactive decay. Further, since we neglect diffusion we are only considering epochs later than ~ 100 days. At these epochs all ^{56}Ni has decayed into ^{56}Co, and we can therefore neglect the first step in this chain.

For $t \gg \tau(^{56}\mathrm{Ni}) = 8.8$ days we need only consider the ^{56}Co decay. Further, we assume that a fraction $(1 - e^{-\tau_\gamma})$ of the gamma-ray energy is trapped in the ejecta. Here τ_γ is an average optical depth to the gamma-rays. Adding the gamma-ray and positron contributions we get

$$L_{bol} = 1.27 \times 10^{42} \left(\frac{M(^{56}\mathrm{Ni})}{0.1 \ \mathrm{M}_\odot} \right) e^{-t/111.3^d} [(1 - e^{-\tau_\gamma}) + 0.035] \ \mathrm{erg \ s^{-1}}. \quad (2.21)$$

The first term in the square bracket represents the gamma-ray input and the second the positron input. As an estimate of the gamma-ray optical depth we take

$$\tau_\gamma = \kappa_\gamma \rho R = \kappa_\gamma \frac{3}{4\pi} \frac{M}{V^2 t^2} \quad (2.22)$$

$$= 0.38 \frac{Z}{A} \left(\frac{M}{\mathrm{M}_\odot} \right) \left(\frac{V}{10^4 \ \mathrm{km \ s^{-1}}} \right)^{-2} \left(\frac{t}{100 \ \mathrm{days}} \right)^{-2} \quad (2.23)$$

We therefore see that the gamma-ray trapping is sensitive to both the mass and the expansion velocity. As an example we take SN 1987A, where most of the gamma-rays were trapped in the core. For the mass we therefore take $M \sim 4$ M$_\odot$ and for the expansion velocity of the core ~ 2000 km s^{-1}. We than get $\tau_\gamma \sim 40(t/100 \ \mathrm{days})^{-2}$. The gamma-rays are therefore in this case trapped up to ~ 600 days. As another extreme case we can take a Type Ia supernova, with $M \sim 1.4$ M$_\odot$, $Z/A \sim 0.5$ and an expansion velocity $\sim 10,000$ km s^{-1}. In this case we get $\tau_\gamma \sim 0.25(t/100 \ \mathrm{days})^{-2}$, and the ejecta is therefore transparent already at ~ 50 days, or earlier for higher ejecta velocities.

Eq. (2.21) shows that for $\tau_\gamma \gtrsim 1$ the bolometric light curve follows the radioactive decay time scale closely, $L_{bol} \propto e^{-t/111.3^d}$. For $0.035 \ll \tau_\gamma \ll 1$ the decay is, however, steeper with $L_{bol} \propto e^{-t/111.3^d}/t^2$. This dependence explains the steeper late light curves of the Type Ia, Ib, and Ic supernovae (§2.2).

From Eq. (2.21) we also see that the positrons become important when $\tau_\gamma \sim 0.035$. For slowly expanding ejecta, as for SN 1987A, the positron contribution does not become important before the next abundant radioactive isotope, ^{57}Ni, dominates the ^{56}Ni contribution. For rapidly expanding supernovae, like Type Ib/c supernovae or Type Ia supernovae, the positron contribution, however, becomes dominant for $t \gtrsim 300 - 500$ days. The bolometric luminosity then again follows the radioactive decay.

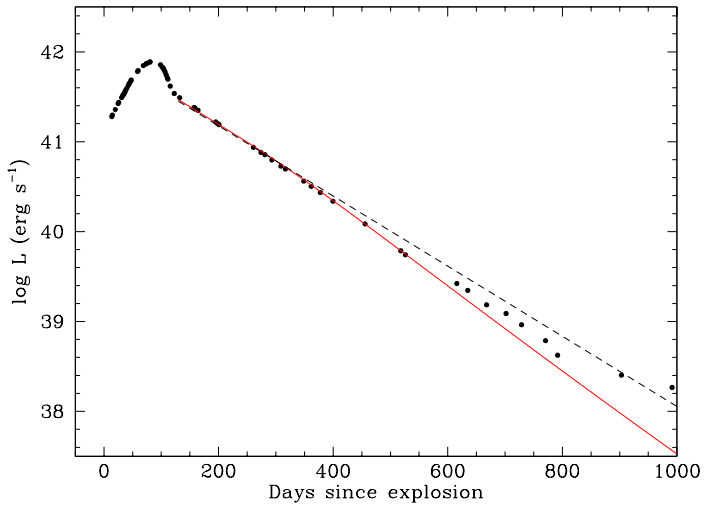

Figure 22: Bolometric light curve from ESO data for SN 1987A during the first 1000 days. The solid line gives the bolometric light curve from Eq. (2.21) with $M(^{56}\mathrm{Ni}) = 0.07$ M$_\odot$ and $\tau_\gamma = 30(t/100^d)^{-2}$. The dashed line shows the total radioactive energy, including that escaping the ejecta. (Data from Bouchet et al. 1990).

2.4.3 The bolometric light curve of SN 1987A

As an example of the usefulness of the bolometric light curve we take SN 1987A. In Fig. 22 we show this during the first 1000 days. After the diffusion phase, which ends by day $\sim$ 130, and up to day $\sim$ 400, the light curve closely follows the predicted linear relation expected for full trapping, $M_{bol} = -t2.5 \log e/111.3^d + \mathrm{const} = -\mathrm{t}/102.5^{\mathrm{d}} + \mathrm{const}$. After day 400 there is an increasing deviation from the full trapping case, well fit by Eq. (2.21) with $\tau_\gamma = 30(t/100^d)^{-2}$, showing that some of the gamma-rays now escape the ejecta. Optical depth unity is reached after $\sim$ 550 days. Most important, from the normalization of the curve one can determine the total nickel mass to $M(^{56}\mathrm{Ni}) = 0.07$ M$_\odot$. The error in this mass is not more than 10%.

By day 600 the bolometric light curve starts to deviate from that predicted by the pure ^{56}Ni decay. This is a clear indication that the next most abundant radioactive isotope ^{57}Ni comes into play. Analysis shows that one finds a good agreement with $M(^{57}\mathrm{Ni}) = 3.3 \times 10^{-3}$ M$_\odot$ (Fig. 23).

Thanks to its very long decay time scale, 89 years, ^{44}Ti takes over as the dominant source of energy to the ejecta at $\sim$ 1700 days. Although only

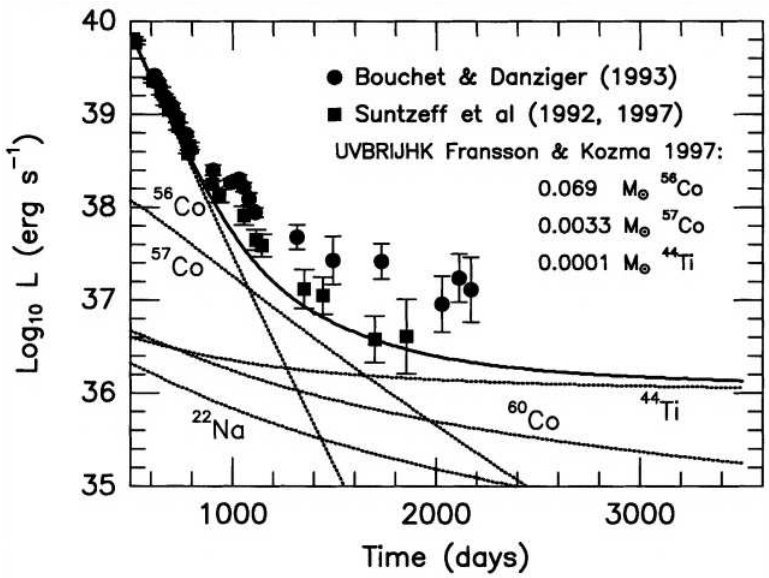

Figure 23: Bolometric light curve for SN 1987A compared to theoretical light curves from different isotopes. (Diehl & Timmes 1998).

$\sim 25\%$ of the energy in the decay is in the form of positrons, these dominate the energy input. The reason is that the positrons are most likely trapped by collisions and even a weak magnetic field, while most of the gamma-rays escape, since $\tau_\gamma \lesssim 0.1$. The trapping in combination with the long decay time scale means that the light curve will be essentially flat after this epoch. Careful modeling by Cecila Kozma shows that a mass of $(1-2) \times 10^{-4}$ $M_\odot$ of ^{44}Ti was formed in the explosion. As we discussed in §2.3, this provides us with a very useful diagnostic of the explosion conditions.

SN 1987A is not the only supernova for which the decays of ^{44}Ti has been observed. For Cas A (age $\sim$ 330 years) COMPTEL on the Compton Gamma Ray Observatory detected the strongest gamma-ray line from the ^{44}Sc at 1.157 MeV (Fig. 24). The strength of the line corresponds to $M(^{44}\mathrm{Ti}) \sim 1.7 \times 10^{-4}$ $M_\odot$, close to that inferred for SN 1987A.

3 Type Ia supernovae

Observationally there are two types of SN explosions, Type I and Type II. The Type I SNe are mainly characterized by the complete lack of hydrogen in their spectra. As we have seen the Type Is can be divided into Type Ia

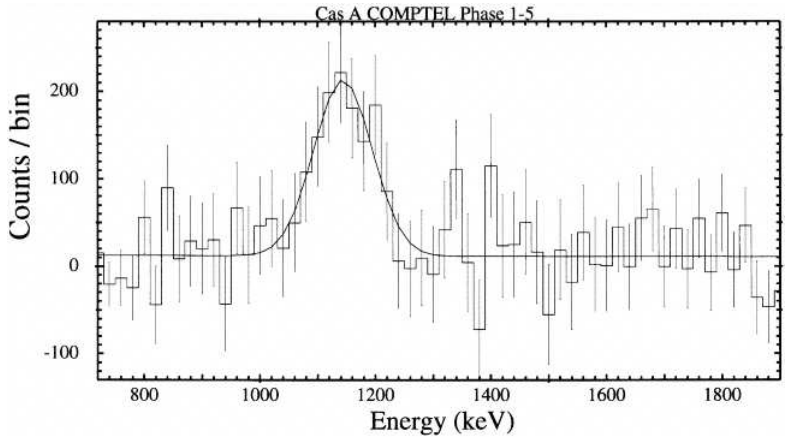

Figure 24: Gamma-ray spectrum of Cas A obtained with COMPTEL on the Compton Gamma Ray Observatory. (Iyudin et al. 1994).

and Type Ib/c. The latter are physically similar to the Type IIs, originating from the collapse of massive stars. The Type Ia SNe have, however, a very different origin, often occurring in elliptical galaxies with a very old stellar population. Observationally they are very similar to each other, both their light curves and spectra. In addition, the absolute luminosities are also similar within a few tenths of a magnitude. They have therefore become the most useful 'standard candle' for determining distances in cosmology.

The extreme uniformity of the Type Ia SNe show that they must come from very similar types of stars. These in addition have to be very old, of the order of billions of years, and can therefore not originate from massive stars, like the core collapse SNe. The standard picture is therefore the explosion of a white dwarf, with mass close to the Chandrasekhar mass. If this is in a close binary system mass transfer from the 'normal' star to the white dwarf may take place. Because of the angular momentum this will spiral in and form a disc around the white dwarf, and later be accreted onto the white dwarf. The accreted gas will then accumulate and normally will after some time explode in explosive nuclear hydrogen burning. This will give rise to an ordinary nova, occurring frequently every year in our Galaxy. In a fairly restrictive range of mass accretion rates, $\gtrsim 10^{-7}$ $M_\odot$ yr^{-1}, the mass of the white dwarf will, however, increase steadily. As the mass increases the radius of the WD will decrease, $R \propto M^{-3}$ (See lecture notes on WDs), and the density will therefore increase. This will heat up the degenerate core and when the density reaches 10^9 g cm^{-3} the nuclear burning will become

explosive.

The ignition of the explosion is still not well understood and may occur in two different modes. Either the nuclear burning will propagate from the ignition site subsonically, with velocity less than the sound velocity, or supersonically, with velocity larger than the sound velocity. In the former case, known as a deflagration, the WD will have time to expand as a result of the increased temperature and pressure, resulting in a decreasing density as the deflagration wave propagates to the surface of the star. The nuclear burning will at the center go all the way to nuclear statistical equilibrium, mainly $M(^{56}\mathrm{Ni}$. As the explosion proceeds and the WD expands the nuclear burning will occur at lower densities and only a partial burning will take place, leading to intermediate mass elements, like Si, S and Ca. In the outer parts of the exploding WD remains of the original carbon and oxygen may be present.

In the supersonic case the pressure of the star does not have time to adjust and the explosion takes place at the density of the original WD. This is known as a detonation. The result of this is that the whole WD, consisting originally of $\sim 50\%$ of carbon and $\sim 50\%$ of oxygen , will be burnt into nuclear statistical equilibrium. This will therefore result in a SN with only iron peak elements.

Observationally one finds that the spectra of Type Ia SNe show clear lines of both oxygen and intermediate mass elements at high velocities, close to the surface. This strongly argues against a pure detonation. Hydrodynamic simulations of pure deflagrations, however, show that in these a substantial amount of unburnt carbon and oxygen occurs also in the center of the supernova. This is in contradiction to observations of Type Ia SNe at late epochs, when the central regions dominate the light. Therefore, a popular model is that of a 'delayed detonation', where the burning stars as a deflagration, expanding the WD. After a few seconds the deflagration will turn into a detonation, transforming the unburnt fuel in the center to higher mass elements. Because the expansion during the deflagration phase leads to a lower density the burning will, however, during the detonation now not go all the way to nuclear statistical equilibrium. A substantial mass of intermediate mass elements will therefore be found at especially high velocities, and even unburned material at the surface.

What causes the transition from deflagration to detonation is however, not understood, and much work remains to be done. Also other aspects of the Type Ia explosions are not well understood. In particular the nature of the progenitor systems are unknown. Only in one case, that of Tychos SN 1572, has a binary companion probably been detected. The mass transfer

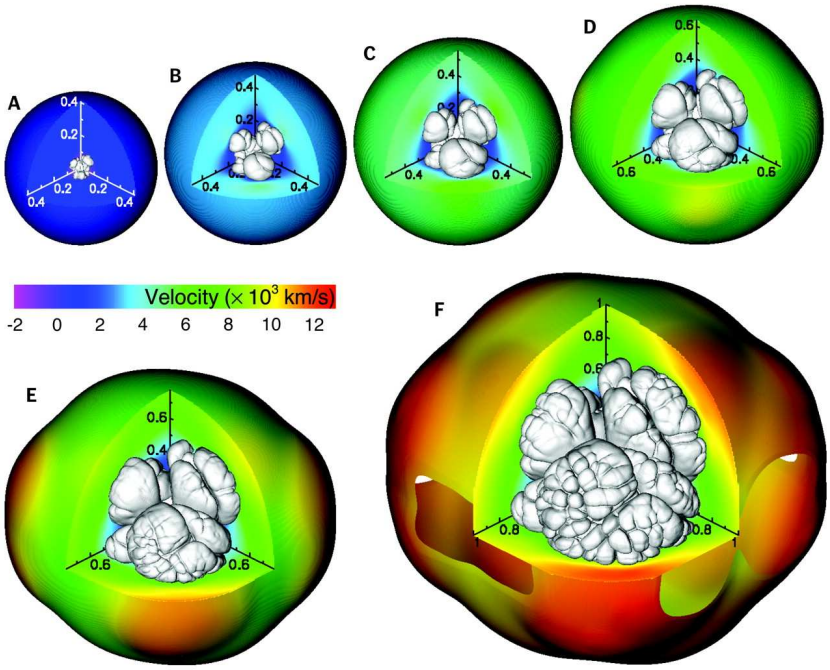

Figure 25: The development of the deflagration flame seen at (A) 1.26, (B) 1.49, (C) 1.57, (D) 1.65, (E) 1.76, and (F) 1.90 s after ignition. The color code shows the velocity. (Gamezo et al. 2003)

process and the accretion is also ill-understood. Most important, the influence of different initial metallicities in the progenitor star, and its effect on especially the C/O ratio is also unknown. This will influence the total nuclear energy available, and therefore the total luminosity of the SN. This is especially serious for the use of Type Ia SNe as cosmological standard candles. The fact that they seem to work so well for this purpose is therefore somewhat surprising and needs to be better understood.

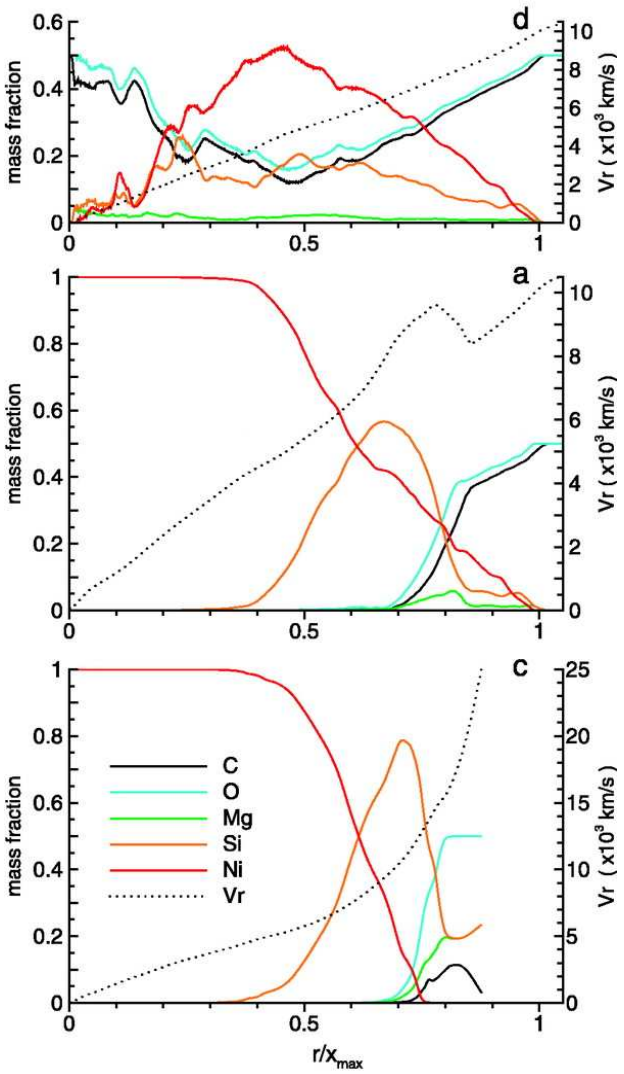

Figure 26: Abundances in one pure deflagration model (top) and two delayed detonation models started at 1.62 s (b) and at 1.51 s (c). Note the absence of oxygen and carbon in the delayed detonation models (Gamezo et al. 2005)